

Pressure-Induced Phase Transitions in Bismutotantalite (BiTaO_4): Insights from Single-Crystal Diffraction and Raman Spectroscopy

Luying Wang, Dongzhou Zhang, Maining Ma, Yi Zhou, Jingui Xu, Dawei Fan,* and Wenge Zhou



Cite This: *Inorg. Chem.* 2025, 64, 5688–5697



Read Online

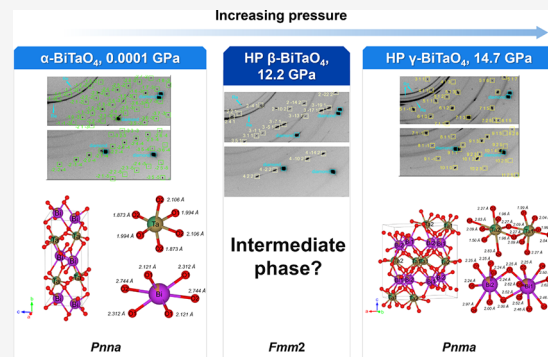
ACCESS |

Metrics & More

Article Recommendations

Supporting Information

ABSTRACT: In situ high-pressure single-crystal X-ray diffraction and Raman spectroscopy analyses were performed on a natural bismutotantalite with an $\alpha\text{-BiTaO}_4$ structure. The results indicate that $\alpha\text{-BiTaO}_4$ transforms into an orthorhombic phase (HP $\gamma\text{-BiTaO}_4$), likely through an intermediate orthorhombic phase (HP $\beta\text{-BiTaO}_4$). The transition pressures are 11.0–11.8 GPa for $\alpha\text{-BiTaO}_4 \rightarrow \text{HP } \beta\text{-BiTaO}_4$ and 13.9–14.4 GPa for $\text{HP } \beta\text{-BiTaO}_4 \rightarrow \text{HP } \gamma\text{-BiTaO}_4$ transition. The phase transitions are reversible. Although the structure of HP $\beta\text{-BiTaO}_4$ was not successfully solved, the possible space group was determined to be $Fmm2$, with unit-cell parameters calculated at 12.2 GPa: $a = 4.8158(18)$ Å, $b = 33.8880(80)$ Å, $c = 5.2910(5)$ Å. In contrast, the structure of HP $\gamma\text{-BiTaO}_4$ was successfully solved and refined at 28.0 GPa, revealing a $Pnma$ space group and unit-cell parameters of $a = 9.8999(12)$ Å, $b = 5.0435(16)$ Å, $c = 10.8331(8)$ Å. The significant volume collapse of 6.2% through the phase transition and the increase in coordination numbers of Bi and Ta from 6 in $\alpha\text{-BiTaO}_4$ to 8/9 in HP $\gamma\text{-BiTaO}_4$ indicate that the HP $\gamma\text{-BiTaO}_4$ structure is considerably more compacted. Additionally, the equation of state for both $\alpha\text{-BiTaO}_4$ and HP $\gamma\text{-BiTaO}_4$ was also studied.



1. INTRODUCTION

Bismuth orthotantalate (BiTaO_4) has drawn the attention of the material science community due to its microwave dielectric and photocatalytic properties.¹ Understanding its various polymorphs is essential for its practical applications.^{2–4} The natural occurrence of BiTaO_4 is in the form of bismutotantalite, a very rare mineral found in granitic pegmatites, which has an orthorhombic structure with a $Pnna$ space group.⁵ Substitutions of Sb for Bi and Nb for Ta are common in natural bismutotantalite.

To date, several polymorphs of BiTaO_4 have been synthesized. Pure synthetic $\alpha\text{-BiTaO}_4$ ($Pnna$) has been reported by several studies since the work of Roth and Waring,⁶ who synthesized this compound from a mixture of bismuth and tantalum oxides by calcination at 1273 K for 18 h. Aurivillius⁷ was the first to synthesize the high-temperature (HT) $\beta\text{-BiTaO}_4$ from a mixture of Bi_2O_3 and Ta_2O_5 at temperatures ranging from 1373 to 1473 K; this polymorph of BiTaO_4 is triclinic with a space group of $P\bar{1}$, based on powder X-ray diffraction (PXRD) results. The HT $\beta\text{-BiTaO}_4$ was subsequently confirmed by several PXRD studies.^{2–4,8} The crystal structure of HT $\beta\text{-BiTaO}_4$ was also validated by single-crystal X-ray diffraction (SCXRD).⁹ Additionally, the results from ref 2 indicated that the phase transition from $\alpha\text{-BiTaO}_4$ to HT $\beta\text{-BiTaO}_4$ is irreversible.

Another HT polymorph of BiTaO_4 is HT $\gamma\text{-BiTaO}_4$. Sleight and Jones were the first to reveal the phase transition from HT $\beta\text{-BiTaO}_4$ to HT $\gamma\text{-BiTaO}_4$ at 998 K using PXRD method.⁸

Their results suggested that the crystal structure of HT $\gamma\text{-BiTaO}_4$ is of the LaTaO_4 type, characterized by a monoclinic structure with a $P2_1/c$ space group.⁸ However, recent HT PXRD experiments² indicated that HT $\gamma\text{-BiTaO}_4$ is orthorhombic with a $Cmcm$ space group, rather than monoclinic with a $P2_1/c$ space group, although the transition temperature (1030 K) for the HT $\beta\text{-BiTaO}_4$ to HT $\gamma\text{-BiTaO}_4$ transition was very similar to that reported in ref 8.

A high-pressure (HP) polymorph of BiTaO_4 has recently been reported, synthesized from HT $\beta\text{-BiTaO}_4$ at 4 GPa and 1573 K.⁴ However, analysis of the PXRD results led to the identification of three possible crystal structures: cubic $Fd\bar{3}m$, cubic $Fm\bar{3}m$ and tetragonal $P4_2/nmc$. In addition, their TEM (transmission electron microscope) results also suggested that the HP BiTaO_4 was a mixture of several phases. The HP BiTaO_4 remains stable up to 973 K at room-pressure but decomposes into a mixture of $\alpha\text{-BiTaO}_4$ and HT $\beta\text{-BiTaO}_4$ at higher temperatures.⁴

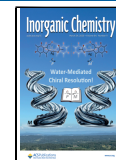
Investigating materials under HP is crucial for enhancing our understanding of their properties, which in turn aids in the

Received: January 17, 2025

Revised: February 27, 2025

Accepted: March 4, 2025

Published: March 12, 2025



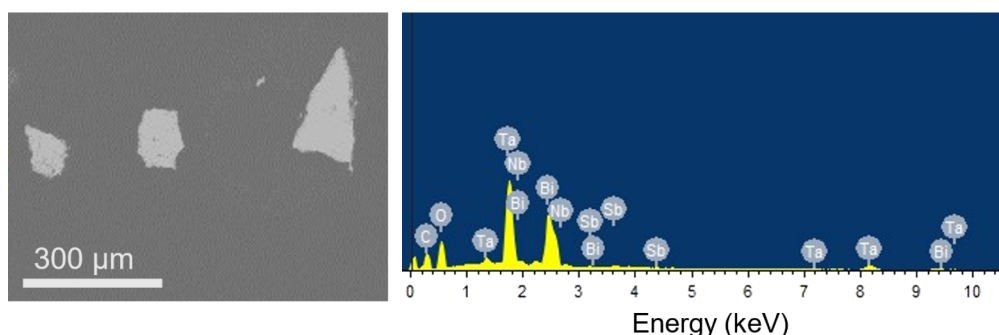


Figure 1. Backscattered image (left) and energy-dispersive spectrum (right) of natural bismutotantalite used in this study.

search for new materials with unique physical properties. HP conditions can modify the physical properties of materials by altering their atomic positions or rearranging the atoms into new structures. For instance, the dielectric constant of HP BiTaO_4 is four times larger than that of HT $\beta\text{-BiTaO}_4$.⁴ To the best of our knowledge, pressure-induced effects on the structure of BiTaO_4 have not yet been well constrained. Therefore, in the present study, we reveal the novel pressure-induced phase transitions of BiTaO_4 using SCXRD and Raman spectroscopy.

2. METHODS

2.1. HP SCXRD Experiments. A natural bismutotantalite of unknown origin was used in this study. A crystal (~ 1 mm in dimension) was fragmented into smaller grains for investigation. Scanning electron microscopy with an energy-dispersive X-ray spectrometer (SEM-EDS) was employed to qualitatively analyze the chemical composition of the carbon-coated crystals (100–200 μm ; Figure 1). The operational conditions included a 15 kV accelerating voltage, a beam current of 3.2–6.8 nA, and a working distance of 10.4 mm.

SCXRD experiments were conducted using a short symmetric diamond-anvil cell (DAC) equipped with two Boehler-Almax-type diamonds (anvil culets with a diameter of 300 μm) and WC seats. A rhenium gasket was preindented to a thickness of approximately 40 μm , and a laser-drilled hole (approximately 180 μm in diameter) in the indented area served as the sample chamber. This DAC setup allowed for a $\pm 32^\circ$ opening angle. A crystal of the sample and several ruby spheres were loaded into the sample chamber (Figure 2). SCXRD data were collected for crystal before the sample chamber was filled with Ne pressure-transmitting medium (PTM) employing the GSECARS/COMPRES gas-loading system.¹⁰ Ruby was utilized as the pressure marker at HP.¹¹

SCXRD experiments were conducted at the GSECARS¹² 13-BM-C beamline¹³ at the Advanced Photon Source, Argonne National Laboratory, using a six-circle diffractometer equipped with a Pilatus3 1M detector.¹⁴ The sample-to-detector distance was 198.34 mm. The wavelength of the monochromatic X-ray beam was 0.434 Å, and LaB_6 powder was used as the diffraction standard. A detailed description of HP SCXRD experiments at 13-BM-C can be found in ref 15. SCXRD images were collected up to 30.5 GPa at a pressure step of ~ 3 GPa, with pressure increased using an automated pressure-driven membrane system. SCXRD images were also collected at five pressure points during decompression to ambient pressure. The SCXRD images were analyzed using the APEX3 crystallography software suite. The ShelX software¹⁶ and the Olex2 user interface¹⁷ were used to solve and refine the crystal structures of the sample after pressure-induced phase transitions. The VESTA software package¹⁸ was employed for the visualization of crystal structures.

2.2. HP Raman Spectroscopy. The confocal micro-Raman system available at GSECARS¹⁹ was utilized to examine the vibrational spectra of the bismutotantalite sample. This Raman system has a spatial resolution of 3 μm , a spectral resolution of 5

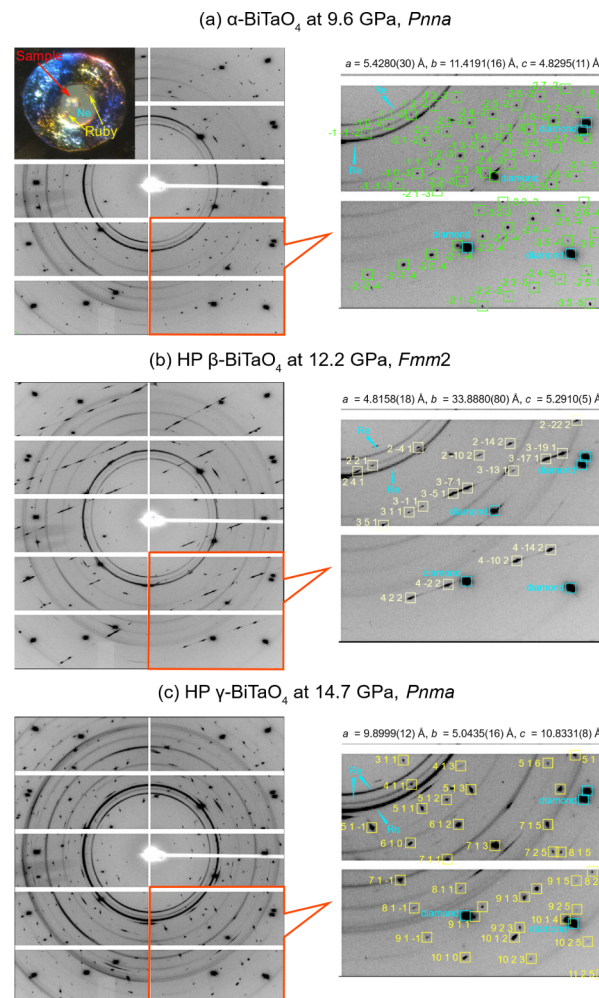


Figure 2. Representative SCXRD images of BiTaO_4 at HP. (a) $\alpha\text{-BiTaO}_4$ at 9.6 GPa; (b) HP $\beta\text{-BiTaO}_4$ at 12.2 GPa; (c) HP $\gamma\text{-BiTaO}_4$ at 14.7 GPa. In each subplot, the left is a whole SCXRD image, and the right shows a zoomed-in region in the left indicated by the red box. The Miller indices are shown for the sample peaks (indicated by colored box), and the diamond and Re peaks are also indicated. The unit-cell parameters are also shown on the right side for each. The inserted figure on the upper left in (a) is a sample photo, showing where are the sample, ruby and Ne.

cm^{-1} , and a laser beam size of 3 μm at the focal point. It is equipped with a spectrometer (Acton SpectraPro SP-2500, Princeton Instrument) featuring gratings with 1800, 1200, and 300 grooves per mm, along with a holographic diffractive bandpass filter from Semrock and a Raman notch filter from OptiGate. Operated in a backscattering configuration, the system employs an apochromatic objective lens and

a 50 μm confocal pinhole to selectively gather spatially filtered backscattered Raman radiation from the specified region of interest. An excitation wavelength of 532 nm was used, generated by a coherent laser (Verdi V2), set at a power level below 20 mW.

The sample was powdered and inserted into a piston–cylinder type DAC equipped with low fluorescence diamond anvils (anvil culets with a diameter of 300 μm) and standard WC seats for HP Raman spectroscopy experiments. The sample chamber (a drilled hole in a rhenium gasket), PTM (Ne) and pressure marker (ruby) were prepared in the same manner as in the SCXRD experiments. The Raman spectra were collected over a frequency range of 100–800 cm^{-1} , following a previous Raman spectroscopic study on $\text{BiTa}_{1-x}\text{Nb}_x\text{O}_4$.²⁰ We collected 16 Raman spectra from room pressure to 27.2 GPa during compression, while 7 spectra were collected during decompression to ambient pressure.

3. RESULTS AND DISCUSSION

3.1. Pressure-Induced Phase Transitions Revealed by SCXRD. The results of the SEM-EDS analysis (Figure 1) indicated that Ta and Bi are the main cations in the sample, while the sample also contains a certain amount of Nb and Sb ($[\text{Bi}_{0.88 \pm 0.02}\text{Sb}_{0.12 \pm 0.02}][\text{Ta}_{0.66 \pm 0.02}\text{Nb}_{0.34 \pm 0.02}]\text{O}_4$, see below). According to the crystal structural studies of natural bismutotantalite by Galliski et al.⁵ Sb and Nb partially substitute Bi and Ta in the structure, respectively. Additionally, they found that structural refinement yields consistent cationic site occupancies with those suggested by electron microprobe analysis. Therefore, we utilized the SCXRD data collected at ambient pressure to refine the crystal structure of our natural bismutotantalite. During the refinement, cations occupying the same polyhedral site (Bi and Sb; Ta and Nb) were set to share the same atomic displacement parameters and fractional coordinates. This resulted in an orthorhombic crystal structure with a *Pnna* space group (Tables 1 and 2), which is consistent

Table 1. Crystallographic Data of the Natural Bismutotantalite, Including $\alpha\text{-BiTaO}_4$ HP $\beta\text{-BiTaO}_4$ and HP $\gamma\text{-BiTaO}_4$ Phases^a

Pressure (GPa)	0.0001	12.2	28.0
Phases	$\alpha\text{-BiTaO}_4$	HP $\beta\text{-BiTaO}_4$	HP $\gamma\text{-BiTaO}_4$
Crystal system	Orthorhombic	Orthorhombic	Orthorhombic
Space group	<i>Pnna</i>	<i>Fmm2</i>	<i>Pnma</i>
<i>a</i> (\AA)	5.6390(3)	4.8158(18)	9.7250(20)
<i>b</i> (\AA)	11.7604(3)	33.8880(80)	4.9540(30)
<i>c</i> (\AA)	4.9617(3)	5.2910(5)	10.5951(13)
<i>V</i> (\AA^3)	329.05(2)	863.50(39)	510.50(20)
Bi site occupancy	0.88(2) Bi + 0.12(2) Sb		
Ta site occupancy	0.66(2) Ta + 0.34(2) Nb		
<i>D</i> _{cal} (g/cm^3)	8.343	-	10.748
<i>R</i> _{int} (%)	3.63	-	3.35
<i>R</i> ₁ (%)	2.21	-	17.65
<i>wR</i> ₂ (%)	6.01	-	39.8
GOOF	1.171	-	1.196

^a— Means not available.

with that of natural bismutotantalite as described by Galliski et al.⁵ This phase has been designated as $\alpha\text{-BiTaO}_4$ in previous studies on the phase relations in the BiTaO_4 system since the work of Roth and Waring.⁶ Furthermore, the refinement of cationic site occupancies resulted in the following values: 0.88(2) for Bi, 0.12(2) for Sb, 0.66(2) for Ta, and 0.34(2) for Nb, leading to a formula of $[\text{Bi}_{0.88 \pm 0.02}\text{Sb}_{0.12 \pm 0.02}][\text{Ta}_{0.66 \pm 0.02}\text{Nb}_{0.34 \pm 0.02}]\text{O}_4$ (Tables 1 and 2). For crystal

Table 2. Fractional Coordinates and Displacement Parameters of Atoms in $\alpha\text{-BiTaO}_4$ at 0.0001 GPa and HP $\gamma\text{-BiTaO}_4$ at 28.0 GPa

atoms	x	y	z	<i>U</i> _{iso}
$\alpha\text{-BiTaO}_4$ at 0.0001 GPa				
Bi1	0.25	0.50	0.72086(10)	0.0073(2)
Ta1	0.35763(6)	0.75	1.25	0.0039(2)
O1	0.4142(6)	0.9025(2)	1.0867(6)	0.0076(9)
O2	0.1399(5)	0.6954(2)	0.9960(8)	0.0089(10)
HP $\gamma\text{-BiTaO}_4$ at 28.0 GPa				
Bi1	0.6227(6)	1.25	0.7671(3)	0.010(1)
Bi2	0.3749(4)	0.75	0.7600(3)	0.003(1)
Ta1	0.6056(8)	0.75	0.5101(4)	0.011(1)
Ta2	0.8550(6)	0.25	0.5073(3)	0.003(1)
O1	0.482(7)	1.00(3)	0.613(4)	0.006(10)
O2	0.229(6)	0.02(2)	0.382(3)	0.002(8)
O3	0.277(7)	0.02(3)	0.616(4)	0.010(10)
O4	0.010(9)	0.25	0.519(5)	0.003(12)
O5	0.565(11)	0.75	0.824(6)	0.010(15)

structure refinements at high pressures, the cationic site occupancies were not varied; instead, they were fixed at the values determined from ambient-pressure structural refinement.

Representative SCXRD images collected at different pressures are shown in Figure 2. Two phase transitions were observed in $\alpha\text{-BiTaO}_4$ up to 30.5 GPa. The analyses indicated that images collected from ambient pressure to 9.6 GPa can be unequivocally assigned to the $\alpha\text{-BiTaO}_4$ structure (Figure 2a). The first phase transition occurs at 12.2 GPa, as indicated by a dramatic change in the diffraction pattern. As shown in Figure 2b, the diffraction pattern exhibits noticeable peak tailing. Analysis of the images and peak indexing suggested a change in the Bravais lattice, moving from the initial primitive lattice of $\alpha\text{-BiTaO}_4$ to a face-centered unit cell. Moreover, the new phase is orthorhombic with a possible space group of *Fmm2* and unit-cell parameters of $a = 4.8158(18)$ \AA , $b = 33.8880(80)$ \AA , and $c = 5.2910(5)$ \AA . We designated this high-pressure phase as HP $\beta\text{-BiTaO}_4$. However, we were unable to solve the structure of HP $\beta\text{-BiTaO}_4$ using the SCXRD data due to limited diffraction peaks and significant peak tailing. The HP $\beta\text{-BiTaO}_4$ is stable within a very limited pressure range (12.2–14.7 GPa). At 14.7 GPa, the second phase transition occurs, as indicated by a dramatic change in the SCXRD image (Figure 2c). In Figure 2c, the diffraction peaks are sharper compared to those in Figure 2b. We designated this phase as HP $\gamma\text{-BiTaO}_4$. The HP $\gamma\text{-BiTaO}_4$ is also orthorhombic, with unit-cell parameters of $a = 9.8999(12)$, $b = 5.0435(16)$, and $c = 10.8331(8)$ \AA at 14.7 GPa. The HP $\gamma\text{-BiTaO}_4$ is stable over a much broader pressure range (14.7–30.5 GPa) compared to HP $\beta\text{-BiTaO}_4$. The structure was solved and refined using the SCXRD data collected at 28.0 GPa, with a space group of *Pnma* (Table 1). Upon decompression, the HP $\gamma\text{-BiTaO}_4$ phase stabilized at 12.4 GPa, then reverted to $\alpha\text{-BiTaO}_4$ at 1.7 GPa (Table 3). We did not collect data at pressures between 12.4 and 1.7 GPa; thus, we cannot rule out the possibility that HP $\beta\text{-BiTaO}_4$ exists during compression.

3.2. Crystal Structure of HP $\gamma\text{-BiTaO}_4$. The crystal structure of HP $\gamma\text{-BiTaO}_4$ was compared with that of $\alpha\text{-BiTaO}_4$ in Figure 3. In the $\alpha\text{-BiTaO}_4$ structure, both Ta and Bi occupy only one symmetrically unique site, while there are two unique sites for O (Figure 3a). Both Ta and Bi are 6-coordinated, with

Table 3. Unit-Cell Parameters and Volumes of Bismutotantalite at Different Pressures^a

Pressure (GPa)	<i>a</i> (Å)	<i>b</i> (Å)	<i>c</i> (Å)	<i>V</i> (Å ³)
0.0001	5.6390(3)	11.7604(3)	4.9617(3)	329.05(2)
0.4(1)	5.6376(3)	11.7410(3)	4.9567(3)	328.09(2)
1.6(1)	5.6143(3)	11.6917(3)	4.9366(3)	324.04(2)
4.3(1)	5.5421(4)	11.5724(4)	4.8996(4)	314.24(2)
7.3(1)	5.4762(4)	11.4736(3)	4.8577(2)	305.22(2)
9.6(1)	5.4280(30)	11.4191(16)	4.8295(11)	299.34(11)
12.2(1)	4.8158(18)	33.8880(80)	5.2910(5)	863.50(39)
14.7(1)	9.8999(12)	5.0435(16)	10.8331(8)	540.90(13)
16.9(1)	9.8619(11)	5.0275(15)	10.7812(7)	534.53(12)
19.4(1)	9.8266(13)	5.0092(17)	10.7354(8)	528.43(14)
22.1(1)	9.7901(16)	4.9920(20)	10.6889(10)	522.33(18)
24.7(1)	9.7572(19)	4.9760(30)	10.6462(11)	516.90(20)
28.0(1)	9.7250(20)	4.9540(30)	10.5951(13)	510.50(20)
30.5(1)	9.7100(30)	4.9390(50)	10.5600(18)	506.50(40)
28.8(1)*	9.7270(20)	4.9570(30)	10.5685(13)	509.60(20)
23.5(1)*	9.7430(60)	5.0260(70)	10.6950(40)	523.70(70)
12.4(1)*	9.9040(20)	5.0290(40)	10.8698(15)	541.40(30)
1.7(1)*	5.6060(90)	11.7450(70)	4.9000(50)	322.60(40)
0.3(1)*	5.6360(70)	11.7630(60)	4.9550(40)	328.50(30)

^a* Indicates decompression data.

Ta–O and Bi–O interatomic distances ranging from 1.873 to 2.106 Å and from 2.121 to 2.744 Å, respectively. By contrast, HP γ -BiTaO₄ has an increased number of symmetrically unique sites, including 2 Bi, 2 Ta, and 5 O (Figure 3b). Both Ta1 and Ta2 are 8-coordinated, forming distorted eight-vertex polyhedra. The interatomic distances in Ta1O₈ and Ta2O₈ are 1.99 to 2.27 Å and 1.50 to 2.83 Å, respectively. Bi1 and Bi2 are coordinated with 9 and 8 oxygen atoms, respectively, with interatomic distances of 2.25 to 2.52 Å in the Bi1O₉ polyhedron and 2.00 to 2.97 Å in the Bi2O₈ polyhedron. The increased coordination of Ta and Bi indicates that the structure of HP γ -BiTaO₄ is much more compact than that of α -BiTaO₄.

The crystal structures of α -BiTaO₄ and the HP γ -BiTaO₄ were also compared layer by layer in Figure 4. In the α -BiTaO₄ structure, the TaO₆ polyhedra are interconnected by sharing one oxygen atom, forming the Ta–O block layers that are parallel to the *ac*-plane (Figure 4(a, top)). The BiO₆ polyhedra form chains parallel to the *a*-axis by sharing two oxygens (Figure 4(a, middle)). These chains are not interconnected but are connected to the TaO₆ polyhedra by sharing one oxygen, which segregates the Ta–O layers and forms the TaO₆–BiO₆ layers parallel to the *bc*-plane (Figure 4(a, bottom)).

In the HP γ -BiTaO₄ structure, the basic layout is similar to that of α -BiTaO₄, with alternating Ta–O and Bi–O layers parallel to the *ab*-plane; however, the connected polyhedra share more oxygens. As shown in Figure 4(b, top), the Ta1O₈ polyhedra are interconnected by sharing two oxygens, while the Ta2O₈ polyhedra are connected to their adjacent Ta1O₈ polyhedra by also sharing two oxygens. Additionally, the Ta2O₈ polyhedra are interconnected by sharing one oxygen. The increased coordination number of Bi in the HP γ -BiTaO₄ structure leads to the interconnection of isolated BiO₆–BiO₆ chains in α -BiTaO₄. As shown in Figure 4(b, middle), the Bi1O₉ polyhedra are connected to the adjacent Bi2O₈ polyhedra by sharing two oxygens, while the Bi1O₉ polyhedra are interconnected by sharing one oxygen. In comparison to

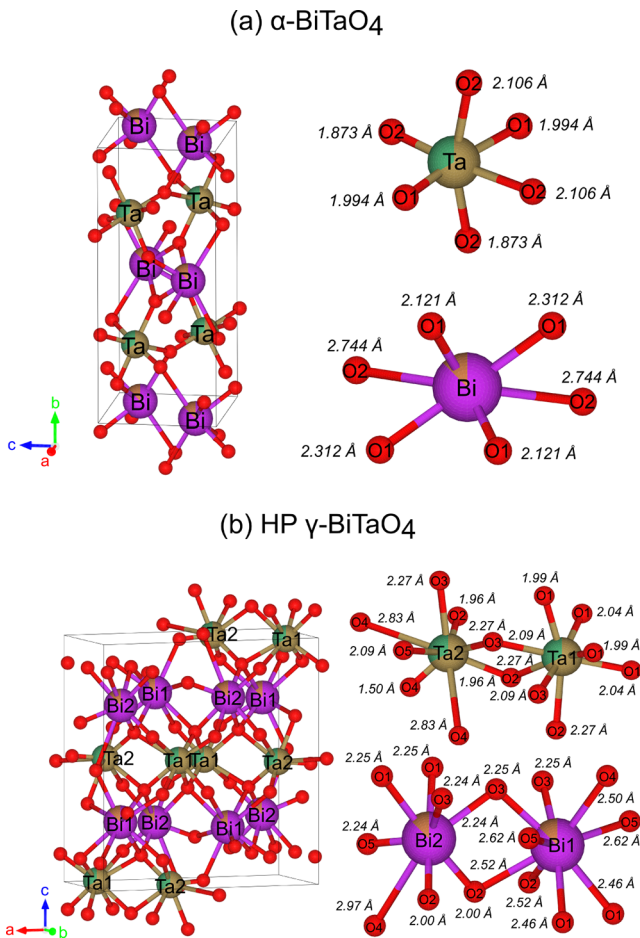


Figure 3. Schematic crystal structures of (a) α -BiTaO₄ and (b) HP γ -BiTaO₄. The left shows the distribution of atoms in a unit-cell; the right shows details of individual Ta–O and Bi–O coordination conditions. The Ta–O and Bi–O interatomic distances are also given. The chemical symbols are shown on the atoms.

those in α -BiTaO₄, the TaO₈ and BiO_{8/9} polyhedra also share more oxygens. As shown in Figure 4(b, bottom), the Ta1O₈ and Bi1O₉ polyhedra, similar to the Ta2O₈ and Bi2O₈, are connected by sharing two oxygens, while the Ta2O₈ and BiO₉ share three oxygens. The decreased bond angles of Ta–O–Ta, Bi–O–Bi, and Ta–O–Bi indicate that HP γ -BiTaO₄ has a more kinked structure than the α -BiTaO₄.

3.3. Compressibility and Equation of State. The unit-cell parameters and volumes for α -BiTaO₄, HP β -BiTaO₄ and HP γ -BiTaO₄ at different pressures are summarized in Table 3 and shown in Figure 5. The decrease in the unit-cell parameters under compression for both α -BiTaO₄ and HP γ -BiTaO₄ is anisotropic. For α -BiTaO₄, the compressibility of the crystal axes decreases in the sequence $a > b > c$ (Figures 5a–c and S1), with their lengths shrinking by 3.7%, 2.9% and 2.7%, respectively, from ambient pressure to 9.6 GPa. However, in the HP γ -BiTaO₄ structure, the *a*-axis is slightly less compressible than the *b*-axis, and both the *a*- and *b*-axis are less compressible than the *c*-axis (Figures 5a–c and S1). From 14.7 to 30.5 GPa, the lengths of *a*, *b*, and *c* change by 1.9%, 2.1% and 2.4%, respectively.

Birch–Murnaghan (BM) equation of state (EOS) with the following form²¹ was used to determine the axial moduli of *a*, *b*, and *c* using the EoSFit7 software.²²

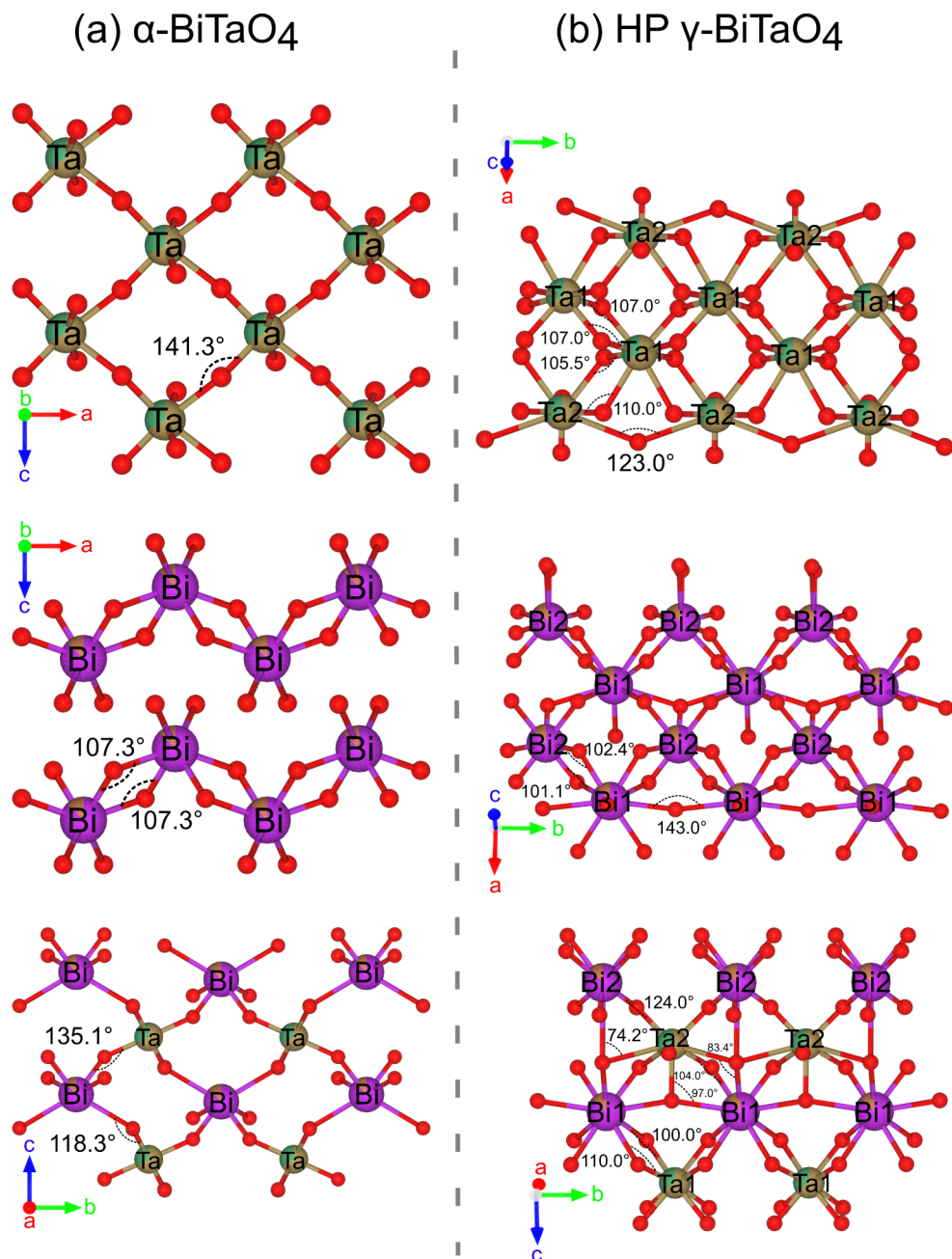


Figure 4. Schematic crystal structures of α -BiTaO₄ (a; left) and HP γ -BiTaO₄ (b; right), separated by the central vertical dashed line, highlighting the layered structures. (a) The TaO₆ (top) and BiO₆ (middle) layers on the *ac*-plane, and the TaO₆–BiO₆ (bottom) layer on the *bc*-plane. (b) The TaO₈ (top) and BiO_{8/9} (middle) layers on the *ab*-plane, and the TaO₈–BiO_{8/9} (bottom) layers on the *bc*-plane. The values of bond angles for Ta–O–Ta, Bi–O–Bi, and Ta–O–Bi are also shown. The Bi and Ta atoms are indicated by their chemical symbols, while the chemical symbols of the oxygens (red ball) are not shown.

$$P = \frac{3K_{T0}}{2} \left[\left(\frac{V_{T0}}{V} \right)^{7/3} - \left(\frac{V_{T0}}{V} \right)^{5/3} \right] \\ \left\{ 1 + \frac{3}{4}(K'_{T0} - 4) \left[\left(\frac{V_{T0}}{V} \right)^{2/3} - 1 \right] \right\} \quad (1)$$

where P , V_{T0} , V , K_{T0} , and K'_{T0} are pressure, unit-cell volume at zero-pressure, unit-cell volume at high pressure, isothermal bulk modulus at zero-pressure, and its pressure derivative, respectively. The volume in eq 1 was replaced with the cube of the unit-cell parameter for EOS fitting. Additionally, the

second-order form (i.e., $K'_{T0} = 4$) of eq 1 was used. The resulting linear moduli for a , b , and c were 210(11) GPa, 252(4) GPa, and 303(4) GPa for α -BiTaO₄, and 511(26) GPa, 506(20) GPa, and 371(9) GPa for HP γ -BiTaO₄, respectively.

Equation 1 was also used to analyze the pressure dependence of the volume of α -BiTaO₄, also using the EoSFit7 software. The determined zero-pressure bulk modulus (K_{T0}) and its pressure derivative (K'_{T0}) are $K_{T0} = 91(7)$ GPa and $K'_{T0} = 1.2(16)$. We also fitted the pressure–volume data to the second-order BM EOS and obtained $K_{T0} = 82(2)$ GPa. The obtained bulk modulus of α -BiTaO₄ is much smaller than that of the α -BiNbO₄ (201 GPa), as determined by DFT

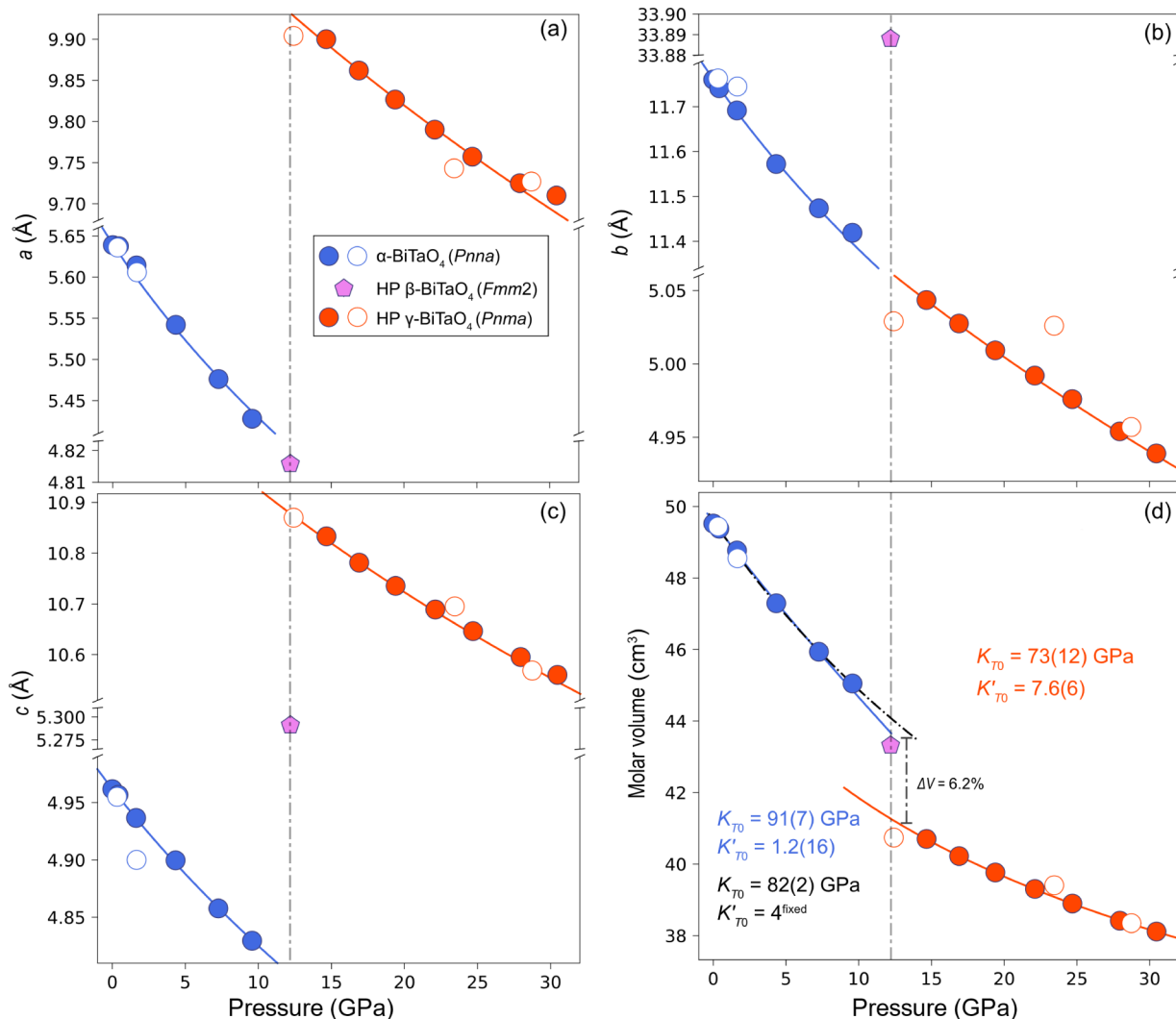


Figure 5. Unit-cell parameters a (a), b (b), and c (c) and molar volume (d) of BiTaO_4 as a function of pressure. The blue, violet, and red circles represent the α - BiTaO_4 , HP β - BiTaO_4 , and HP γ - BiTaO_4 , respectively. The filled and unfilled symbols represent data collected during compression and decompression, respectively. The solid lines in (a–c) represent a second-order BM EOS fitting of the data; while in (d) the blue solid line represents a third-order BM EOS fitting, the dash-dot line represents a second-order BM EOS fitting, and the red line represents a Murnaghan EOS fitting. The bulk modulus (K_{T0}) and its pressure derivative (K'_{T0}) are shown for the α - BiTaO_4 and HP γ - BiTaO_4 in (d).

calculations reported in ref 23. This indicates that the substitution of Nb for Ta would lower the compressibility of α - BiTaO_4 . The Murnaghan EOS²² was used to fit the pressure–volume data of the HP γ - BiTaO_4 , as fitting with the third-order BM EOS failed to yield reliable values for K_{T0} and K'_{T0} . The results were $K_{T0} = 73(12)$ GPa and $K'_{T0} = 7.6(6)$, indicating that HP γ - BiTaO_4 is less compressible compared to α - BiTaO_4 . The volume collapse is significant (6.2%) during the phase transition (Figure 5d), indicating a much more compact structure for HP γ - BiTaO_4 (Figures 3–5).

3.4. Pressure-Induced Phase Transitions Revealed by Raman Spectroscopy. The Raman spectrum collected at ambient pressure matches well with those of natural bismutotantalite (RRUFF ID: R130778) and synthetic α - BiTaO_4 .²⁰ Twelve Raman peaks (ν_1 – ν_2 and ν_4 – ν_{13}) distributed between 100 and 800 cm^{−1} are identified at ambient pressure (Figure 6). Based on previous vibrational spectroscopic studies of BiTaO_4 ²⁰ and its analogues (e.g., BiNbO_4 ,^{24–26} SbNbO_4 ,^{24,25} the Raman peaks observed for α

BiTaO_4 in this study can be assigned to specific vibrational modes as follows. The peaks (ν_1 – ν_2) below 200 cm^{−1} correspond to lattice modes. Among the remaining peaks, the strongest (ν_{12} , ~620 cm^{−1}) represents the symmetric Ta–O stretching vibration of the TaO_6 octahedra, while the peak at a slightly lower frequency (ν_{11} , ~550 cm^{−1}) corresponds to another Ta–O stretching mode (likely asymmetric stretching mode) relevant to the TaO_6 octahedra. The relatively weak peaks at frequencies higher than ν_{12} originate from Bi–O stretching vibrations. The peaks (ν_4 – ν_6) between 200 and 300 cm^{−1} represent bending vibrations relevant to the BiO_6 and TaO_6 octahedra, and those (ν_7 – ν_{10}) between 300 and 500 cm^{−1} arise from combined stretching and bending vibrations relevant to the BiO_6 and TaO_6 octahedra.

As the pressure is increased to 0.4 GPa, all the peaks can be identified at their appropriate positions, but three peaks (ν_8 – ν_{10}) between 370 and 450 cm^{−1} are weakened (Figure 6a). When the pressure is increased to 6.5 GPa, ν_8 and ν_{11} disappear (Figure 7a,b), ν_4 , ν_5 and ν_7 weaken, whereas the intensity of ν_9 remarkably increases, and a clear shoulder (ν_3)

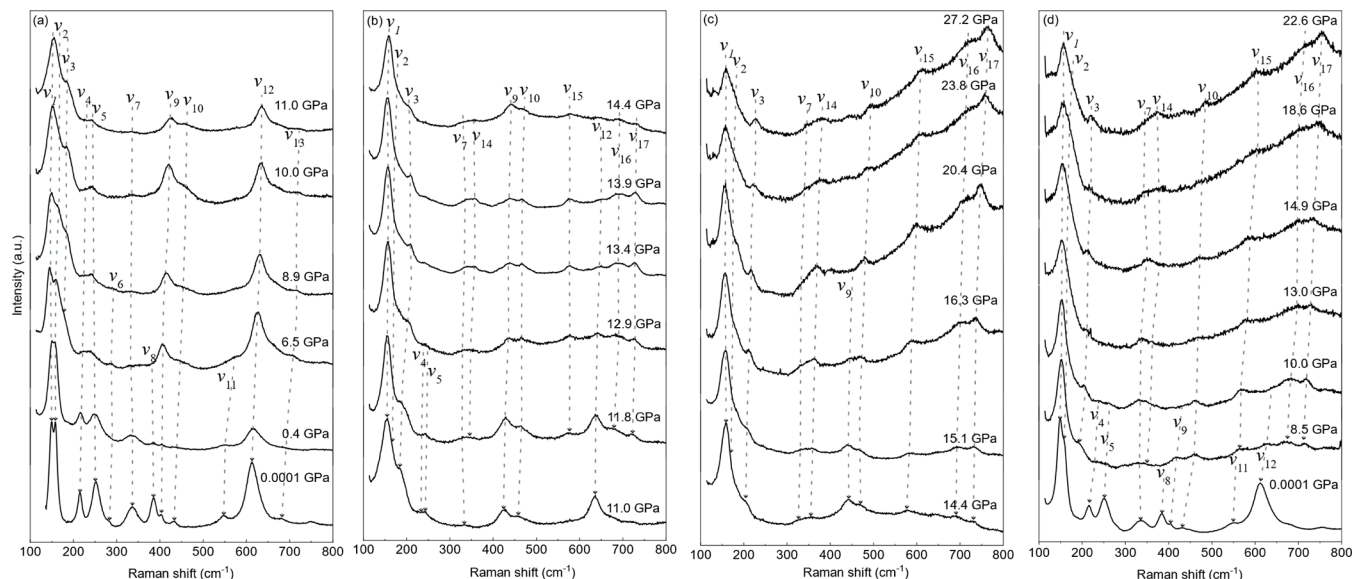


Figure 6. Raman spectra of bismutotantalite collected during compression (a–c; 0.0001–11.0 GPa, 11.0–14.4 GPa, and 14.4–27.2 GPa) and decompression (d; 22.6–0.0001 GPa). The arrows are shown to outline the evolution of each Raman peak (ν_1 – ν_{17}).

appears on ν_2 . At pressures between 6.5 and 11.0 GPa, the Raman peaks exhibit no remarkable changes except for the disappearance of ν_6 at 8.9 GPa and of ν_{13} at 11.0 GPa (Figures 6a and 7a,b). Upon further increasing the pressure, observable changes occur at pressures between 11.8 and 14.4 GPa (Figure 6b). Four new peaks (ν_{14} – ν_{17}) appear at 11.8 GPa (Figure 7a,b), and two peaks (ν_4 – ν_5) disappear at 12.9 GPa (Figure 7c). Additionally, ν_9 and ν_{12} weaken at pressures higher than 11.8 GPa compared to those at pressures below 12.9 GPa, and ν_{12} disappears at 14.4 GPa. Between 14.4 and the maximum pressure of 27.2 GPa, no remarkable changes occur except for the disappearance of ν_9 at 20.4 GPa (Figures 6c and 7a). Upon decompression to ambient pressure, the Raman spectrum returns to its original appearance under ambient conditions (Figure 6d).

3.5. Pressure-Induced Phase Transitions in Bismutotantalite and Their Comparison with Synthetic BiNbO₄. Our HP SCXRD data indicate that the first transition (α -BiTaO₄ \rightarrow HP β -BiTaO₄) occurs at a pressure between 9.6 and 12.2 GPa, while the second transition (HP β -BiTaO₄ \rightarrow HP γ -BiTaO₄) takes place between 12.2 and 14.7 GPa. The observable changes in the Raman spectrum with increasing pressure below 8.9 GPa (Figures 6a and 7), including the weakening of peaks ν_4 , ν_5 , ν_7 and ν_8 ; the appearance of peak ν_3 ; the disappearance of peaks ν_6 , ν_8 and ν_{11} ; as well as inflections in pressure-Raman shift dependence for peaks ν_1 , ν_2 , ν_5 , ν_9 and ν_{10} at 6.5 GPa may suggest local structural distortions not detected by XRD. Additionally, new Raman peaks (ν_{14} – ν_{17} ; Figure 6b) appearing at 11.8 GPa along with inflections in pressure-Raman shift dependence for peaks ν_3 and ν_4 (Figure 7c) likely correspond to the α -BiTaO₄ \rightarrow HP β -BiTaO₄ transition revealed by SCXRD. The complete disappearance of peak ν_{12} —a strong peak for α -BiTaO₄ at ambient pressure—and inflections in pressure-Raman shift dependence for peaks ν_3 and ν_7 at 14.4 GPa (Figure 7b,c) indicate the structure transition from HP β -BiTaO₄ to HP γ -BiTaO₄. Both the Raman (11.0–14.4 GPa) and SCXRD (9.6–14.7 GPa) data suggest that the HP β -BiTaO₄ phase is stable only within a very narrow pressure region.

Consistent with our SCXRD data, our Raman data also indicate two pressure-induced phase transitions. At ambient pressure, apart from the Raman peaks corresponding to lattice modes, the strongest Raman peak is ν_{12} , originating from the symmetric Ta–O stretching mode of the TaO₆ octahedra. Based on the crystal structure, TaO₆ octahedra in α -BiTaO₄ are not greatly distorted from an ideal octahedron, whereas BiO₆ octahedra are highly distorted, as indicated by the distortion indices: 0.039 for TaO₆ and 0.098 for BiO₆. Consequently, we can detect a strong Raman peak for Ta–O symmetric stretching mode (Figure 6). As the pressure increases, one of the notable changes in the Raman spectrum is the weakening of the ν_{12} mode, especially at pressures exceeding 11.8 GPa. This suggests that the symmetry of the initially slightly distorted TaO₆ octahedra decreases with increasing pressure, consistent with our SCXRD data. The coordination number of Ta is 6 for α -BiTaO₄ and 8 for HP γ -BiTaO₄ (Figure 3), indicating that the initial TaO₆, which is relatively close to an ideal octahedron, is absent in the structure of HP γ -BiTaO₄. We also note that despite its rapid weakening, ν_{12} mode remains identifiable at pressures between 11.8 and 14.4 GPa, possibly indicating that the coordination number of Ta increases gradually within the HP β -BiTaO₄ region. Furthermore, ν_{12} disappears completely only when the pressure is increased to 14.4 GPa, indicating the complete phase transition to HP γ -BiTaO₄. Given the Raman spectral similarity between HP β -BiTaO₄ and HP γ -BiTaO₄ (Figure 6), it is plausible that the HP β -BiTaO₄ phase is an intermediate phase through which α -BiTaO₄ transforms into HP γ -BiTaO₄. The occurrence of an intermediate phase during pressure-induced phase transitions is not uncommon. For instance, at 5–6 GPa, U₃O₈ undergoes a phase transition to a fluorite phase through an intermediate tetragonal phase.²⁷ Similarly, theoretical calculations have reported that SiC transitions from a zinc blende to a rocksalt structure through an orthorhombic intermediate phase at high pressure.²⁸

Recently, Dong et al.²⁹ reported pressure-induced phase transitions in α -BiNbO₄ (isostructural with bismutotantalite), as revealed by in situ PXRD and Raman spectroscopy up to 39.7 GPa. They found that α -BiNbO₄ transforms into a

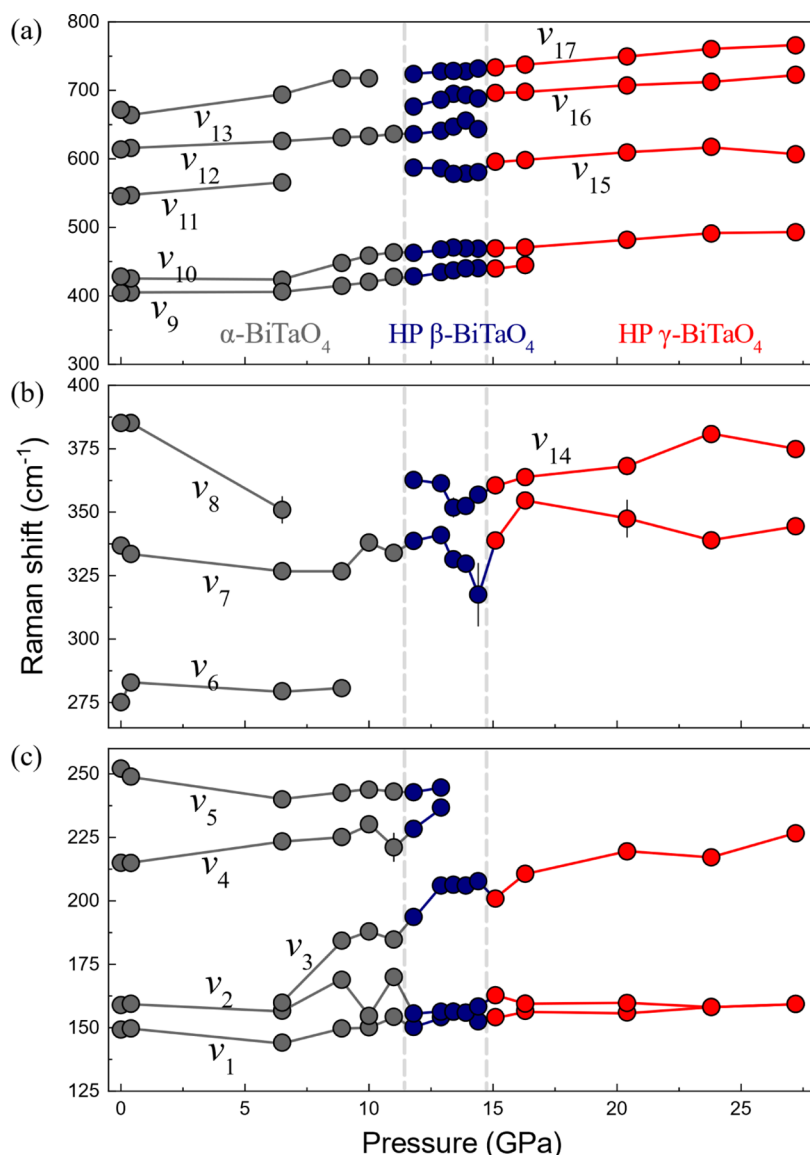


Figure 7. Raman shifts of α -BiTaO₄ (gray), HP β -BiTaO₄ (blue), and HP γ -BiTaO₄ (red) as a function of pressure. Error bars may be smaller than the symbol size.

monoclinic $C2/c$ phase at 10.3 GPa, which differs from the structures of HP β -BiTaO₄ and HP γ -BiTaO₄ observed in this study. As they did not provide detailed crystal structural information for the $C2/c$ phase, a direct structural comparison is not possible. The compositional difference between their sample and ours may account for the discrepancies between their HP phase and those observed herein. Although our sample was Nb-bearing, it was BiTaO₄-dominant, whereas their sample was pure BiNbO₄. Indeed, prior studies,^{4,30,31} have suggested that the HP phase transition behavior of BiNbO₄ differs from that of BiTaO₄. For instance, while β -BiNbO₄ transforms into a single HP phase (HP BiNbO₄; cubic Sm₂Sn₂O₇-type structure³¹) at pressures of 3–5 GPa and temperatures of 1073–1673 K³⁰, β -BiNbO₄ does not transform into a single phase under similar high-pressure and high-temperature conditions; rather the resulting product is a mixture of several phases.⁴ Therefore, we attribute the different HP phases observed in our Nb-bearing BiTaO₄ compared to the BiNbO₄ reported by Dong et al.²⁹ primarily to this compositional difference. Furthermore, Dong et al.²⁹ employed

Ar as their PTM, whereas Ne was used in this study. Ar and Ne behave very differently in maintaining hydrostatic pressure conditions at pressures higher than 10 GPa,³² where the phase transitions of bismutontantalite and α -BiNbO₄ occur. This may also contribute to the differences in the HP phases of bismutontantalite.

4. CONCLUSIONS

This study presents the pressure-induced phase transitions of a natural bismutontantalite (α -BiTaO₄ structure) revealed by in situ HP SCXRD and Raman spectroscopic experiments. We observed the following phase transitions with increasing pressure: α -BiTaO₄ (*Pnma*) \rightarrow HP β -BiTaO₄ (*Fmm2*, 12.2 GPa) \rightarrow HP γ -BiTaO₄ (*Pnma*, 14.4 GPa). The HP β -BiTaO₄ phase is stable within a very narrow pressure region, and it may be an intermediate phase, while the HP γ -BiTaO₄ is stable up to the maximum pressure of 30.5 GPa. These phase transitions are reversible; however, we did not observe HP β -BiTaO₄ during decompression. Although we were unable to solve the structure of the HP β -BiTaO₄ phase due to poor data quality,

we successfully solved and refined the structure of the HP γ -BiTaO₄ phase using SCXRD data collected at 28.0 GPa. The results indicate that the HP γ -BiTaO₄ phase is much more compact than α -BiTaO₄, due to the increase in the coordination numbers of Bi and Ta from 6 in the latter to 8/9 in the former.

ASSOCIATED CONTENT

Supporting Information

The Supporting Information is available free of charge at <https://pubs.acs.org/doi/10.1021/acs.inorgchem.Sc00260>.

a/b and *a/c* ratios of BiTaO₄ as a function of pressure
(PDF)

Accession Codes

Deposition Numbers 2417473–2417474 contain the supplementary crystallographic data for this paper. These data can be obtained free of charge via the joint Cambridge Crystallographic Data Centre (CCDC) and Fachinformationszentrum Karlsruhe [Access Structures service](#).

AUTHOR INFORMATION

Corresponding Author

Dawei Fan – State Key Laboratory of Critical Mineral Research and Exploration, Institute of Geochemistry, Chinese Academy of Sciences, Guiyang 550081, China; Key Laboratory of High-Temperature and High-Pressure Study of the Earth's Interior, Institute of Geochemistry, Chinese Academy of Sciences, Guiyang, Guizhou 550081, China;
Email: fandawei@mail.gyig.ac.cn

Authors

Luying Wang – School of Management, Guizhou University of Commerce, Guiyang 550014, China; orcid.org/0009-0007-2608-3181

Dongzhou Zhang – GeoSoilEnviroCARS, University of Chicago, Argonne, Chicago, Illinois 60437, United States

Maining Ma – National Key Laboratory of Earth System Numerical Modeling and Application, University of Chinese Academy of Sciences, Beijing 101408, China

Yi Zhou – School of Geoscience and Technology, Southwest Petroleum University, Chengdu, Sichuan 610500, China

Jingui Xu – State Key Laboratory of Critical Mineral Research and Exploration, Institute of Geochemistry, Chinese Academy of Sciences, Guiyang 550081, China; Key Laboratory of High-Temperature and High-Pressure Study of the Earth's Interior, Institute of Geochemistry, Chinese Academy of Sciences, Guiyang, Guizhou 550081, China

Wenge Zhou – Key Laboratory of High-Temperature and High-Pressure Study of the Earth's Interior, Institute of Geochemistry, Chinese Academy of Sciences, Guiyang, Guizhou 550081, China

Complete contact information is available at:

<https://pubs.acs.org/10.1021/acs.inorgchem.Sc00260>

Notes

The authors declare no competing financial interest.

ACKNOWLEDGMENTS

Sincere thanks go to S.N. Tkachev for his help with gas loading, and to Stella Chariton for her help with the Raman experiments. This project was supported by the Hundred Talents Program of the Chinese Academy of Sciences, the

National Natural Science Foundation of China (grant no. 42172048), the Guizhou Provincial Science and Technology Projects (QKHPTRC-YQK[2023]035, QKHJC-ZK[2021]ZD042, QKHJC-ZK[2021]YB216, and QKHPTKXJZ[2024]006), and the National Foundation for Guiding Local Science and Technology Development (Guizhou [2024] 043). Y.Z. acknowledges support from the National Natural Science Foundation of China (grant no. 42302114). Portions of this work were supported by GSECARS through NSF grant EAR-1634415. This research used resources of the Advanced Photon Source; a U.S. Department of Energy (DOE) Office of Science User Facility operated for the DOE Office of Science by Argonne National Laboratory under contract no. DE-AC02-06CH11357.

REFERENCES

- (1) (a) Huang, C.-L.; Weng, M.-H. Low-fire BiTaO₄ dielectric ceramics for microwave applications. *Mater. Lett.* **2000**, *43* (1), 32–35. (b) Nguyen, Q. B.; Vu, D. P.; Nguyen, T. H. C.; Doan, T. D.; Pham, N. C.; Duong, T. L.; Tran, D. L.; Bach, G. L.; Tran, H. C.; Dao, N. N. Photocatalytic Activity of BiTaO₄ Nanoparticles for the Degradation of Methyl Orange Under Visible Light. *J. Electron. Mater.* **2019**, *48* (5), 3131–3136.
- (2) Zhuk, N. A.; Krzhizhanovskaya, M. G.; Belyy, V. A.; Kharton, V. V.; Chichineva, A. I. Phase Transformations and Thermal Expansion of α - and β -BiTaO₄ and the High-Temperature Modification γ -BiTaO₄. *Chem. Mater.* **2020**, *32* (13), 5493–5501.
- (3) Zhuk, N. A.; Krzhizhanovskaya, M. G.; Belyy, V. A.; Sekushin, N. A.; Chichineva, A. I. The bismuth orthotantalate with high anisotropic thermal expansion. *Scr. Mater.* **2019**, *173*, 6–10.
- (4) Zhou, D.; Fan, X. Q.; Jin, X. W.; He, D. W.; Chen, G. H. Structures, Phase Transformations, and Dielectric Properties of BiTaO₄ Ceramics. *Inorg. Chem.* **2016**, *55* (22), 11979–11986.
- (5) Galliski, M. A.; Márquez-Zavalía, M. F.; Cooper, M. A.; Cerny, P.; Hawthorne, F. C. Bismutotantalite from northwestern Argentina: Description and crystal structure. *Can. Mineral.* **2001**, *39* (1), 103–110.
- (6) Roth, R. S.; Waring, J. L. Synthesis and stability of bismutotantalite, stibiotantalite and chemically similar ABO₄ compounds. *Am. Mineral.* **1963**, *48* (11–12), 1348–1356.
- (7) Aurivillius, B. X-ray investigations on BiNbO₄, BiTaO₄ and BiSbO₄. *Ark. Kemi* **1951**, *3* (2–3), 153–161.
- (8) Sleight, A.; Jones, G. Ferroelastic transitions in β -BiNbO₄ and β -BiTaO₄. *Acta Crystallogr., Sect. B: Struct. Crystallogr. Cryst. Chem.* **1975**, *31* (11), 2748–2749.
- (9) Muktha, B.; Darriet, J.; Madras, G.; Guru Row, T. N. Crystal structures and photocatalysis of the triclinic polymorphs of BiNbO₄ and BiTaO₄. *J. Solid State Chem.* **2006**, *179* (12), 3919–3925.
- (10) Rivers, M.; Prakapenka, V. B.; Kubo, A.; Pullins, C.; Holl, C. M.; Jacobsen, S. D. The COMPRES/GSECARS gas-loading system for diamond anvil cells at the Advanced Photon Source. *High Pressure Res.* **2008**, *28* (3), 273–292.
- (11) Mao, H.; Xu, J.-A.; Bell, P. Calibration of the ruby pressure gauge to 800 kbar under quasi-hydrostatic conditions. *J. Geophys. Res.* **1986**, *91* (B5), 4673–4676.
- (12) Sutton, S. R.; Rivers, M. L.; Chariton, S.; Eng, P. J.; Lanzirotti, A.; Newville, M.; Officer, T.; Prakapenka, V. B.; Ryu, Y. J.; Stubbs, J. E.; Tkachev, S.; Wang, Y.; Wanhalala, A.; Xu, J.; Xu, M.; Yu, T.; Zhang, D. GeoSoilEnviroCARS (Sector 13) at the Advanced Photon Source: A comprehensive synchrotron radiation facility for Earth science research at ambient and extreme conditions. *Phys. Chem. Miner.* **2022**, *49* (8), 32.
- (13) Xu, J.; Zhang, D.; Tkachev, S. N.; Dera, P. K. Partnership for eXtreme Xtallography (PX2)—A state-of-the-art experimental facility for extreme-conditions crystallography: A case study of pressure-induced phase transition in natural ilvaite. *Matter Radiat. Extremes* **2022**, *7* (2), 028401.

- (14) Zhang, D.; Xu, J.; Dera, P. K.; Rivers, M. L.; Eng, P. J.; Prakapenka, V. B.; Stubbs, J. E. Recent developments on high-pressure single-crystal X-ray diffraction at the Partnership for eXtreme Xtallography (PX2) program. *Phys. Chem. Miner.* **2022**, *49* (6), 19.
- (15) Zhang, D.; Dera, P. K.; Eng, P. J.; Stubbs, J. E.; Zhang, J. S.; Prakapenka, V. B.; Rivers, M. L. High Pressure Single Crystal Diffraction at PX². *J. Visualized Exp.* **2017**, No. e54660.
- (16) Sheldrick, G. M. A short history of SHELX. *Acta Crystallogr., Sect. A: Found. Crystallogr.* **2008**, *64* (1), 112–122.
- (17) Dolomanov, O. V.; Bourhis, L. J.; Gildea, R. J.; Howard, J. A.; Puschmann, H. OLEX2: A complete structure solution, refinement and analysis program. *J. Appl. Crystallogr.* **2009**, *42* (2), 339–341.
- (18) Momma, K.; Izumi, F. VESTA 3 for three-dimensional visualization of crystal, volumetric and morphology data. *J. Appl. Crystallogr.* **2011**, *44* (6), 1272–1276.
- (19) Holtgrewe, N.; Greenberg, E.; Prescher, C.; Prakapenka, V. B.; Goncharov, A. F. Advanced integrated optical spectroscopy system for diamond anvil cell studies at GSECARS. *High Pressure Res.* **2019**, *39* (3), 457–470.
- (20) Lee, C.-Y.; Macquart, R.; Zhou, Q.; Kennedy, B. J. Structural and spectroscopic studies of BiTa_{1-x}Nb_xO₄. *J. Solid State Chem.* **2003**, *174* (2), 310–318.
- (21) Birch, F. Finite elastic strain of cubic crystals. *Phys. Rev.* **1947**, *71* (11), 809–824.
- (22) Angel, R. J.; Gonzalez-Platas, J.; Alvaro, M. EosFit7c and a Fortran module (library) for equation of state calculations. *Z. Kristallogr. -Cryst. Mater.* **2014**, *229* (5), 405–419.
- (23) Litimein, F.; Khenata, R.; Gupta, S. K.; Murtaza, G.; Reshak, A. H.; Bouhemadou, A.; Bin Omran, S.; Yousaf, M.; Jha, P. K. Structural, electronic, and optical properties of orthorhombic and triclinic BiNbO₄ determined via DFT calculations. *J. Mater. Sci.* **2014**, *49* (22), 7809–7818.
- (24) Ayyub, P.; Multani, M. S.; Palkar, V. R.; Vijayaraghavan, R. Vibrational spectroscopic study of ferroelectric SbNbO₄, antiferroelectric BiNbO₄, and their solid solutions. *Phys. Rev. B* **1986**, *34* (11), 8137–8140.
- (25) Ayyub, P.; Palkar, V. R.; Multani, M. S.; Vijayaraghavan, R. Structural, dielectric and vibrational properties of the stibiotantalite (Sb_{1-x}Bix)NbO₄ system for 0 ≤ x ≤ 1. *Ferroelectrics* **1987**, *76* (1), 93–106.
- (26) Hossain, M. Z.; Nishat, S. S.; Ahmed, S.; Hossain, Q. S.; Khan, M. N. I.; Hasan, T.; Bashar, M. S.; Hossain Faysal, A. K. M. S.; Syed, I. M.; Hossain, K. S.; et al. Combined experimental and DFT approach to BiNbO₄ polymorphs. *RSC Adv.* **2023**, *13* (8), 5576–5589.
- (27) Shukla, B.; Kumar, N. R. S.; Maji, D.; Chakraborty, S.; Upadhyay, A.; Srihari, V.; Ravindran, T. R.; Shekar, N. V. C. Pressure-induced phase transition, its mechanism and compressibility studies on nanocrystalline and bulk U₃O₈. *J. Solid State Chem.* **2023**, *328*, 124340.
- (28) Catti, M. Orthorhombic Intermediate State in the Zinc Blende to Rocksalt Transformation Path of SiC at High Pressure. *Phys. Rev. Lett.* **2001**, *87* (3), 035504.
- (29) Dong, X.; Huangfu, Z.; Feng, S.; Liang, Y.; Zhang, H.; Zhu, X.; Yang, K.; Wang, Z.; Cheng, X.; Su, L. Pressure-induced phase transition in α-and β-BiNbO₄. *Phys. Chem. Chem. Phys.* **2022**, *24* (34), 20546–20552.
- (30) Xu, C.; He, D.; Liu, C.; Wang, H.; Zhang, L.; Wang, P.; Yin, S. High pressure and high temperature study the phase transitions of BiNbO₄. *Solid State Commun.* **2013**, *156*, 21–24.
- (31) Liu, Y.-J.; Zhang, J.-W.; He, D.-W.; Xu, C.; Hu, Q.-W.; Qi, L.; Liang, A.-K. Exploring the compression behavior of HP-BiNbO₄ under high pressure. *Chin. Phys. B* **2017**, *26*, 116202.
- (32) Klotz, S.; Chervin, J.; Munsch, P.; Le Marchand, G. Hydrostatic limits of 11 pressure transmitting media. *J. Phys. D: Appl. Phys.* **2009**, *42* (7), 075413.